

Supplementary Information to:

Floating hollow carbon spheres for improved solar evaporation

A. Celzard^{1*}, A. Pasc², S. Schaefer¹, K. Mandel^{3,4}, T. Ballweg³,
S. Li², G. Medjahdi⁵, V. Nicolas¹ and V. Fierro¹

¹ Université de Lorraine, CNRS, IJL, F-88000 Epinal, France

² Université de Lorraine, CNRS, L2CM, F-54000 Nancy, France

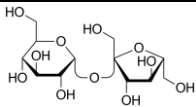
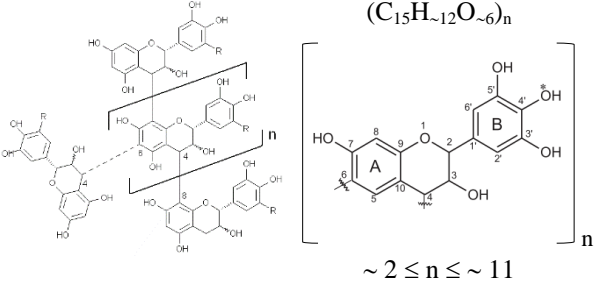
³ Fraunhofer Institute for Silicate Research ISC, D-97082 Würzburg, Germany

⁴ Chair of Chemical Technology of Materials Synthesis, Department Chemistry and Pharmacy, Julius-Maximilians-Universität Würzburg Röntgenring 11, 97070 Würzburg, Germany

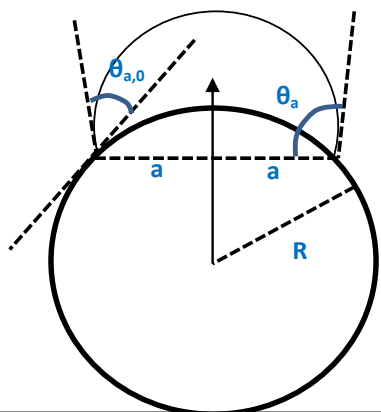
⁵ Université de Lorraine, CNRS, IJL, F-54000 Nancy, France

* Corresponding author. Tel: + 33 372 74 96 14. Fax: + 33 372 74 96 38. E-mail address : alain.celzard@univ-lorraine.fr (A. Celzard)

Table S11. Information about the carbon precursors used in the hydrothermal treatment.

Precursor	Chemical structure	Molecular formula	Molecular weight (g mol ⁻¹)	Supplier	Commercial reference
Sucrose		C ₁₂ H ₂₂ O ₁₁	342.30	Sigma-Aldrich	S-7903
Mimosa tannin		(C ₁₅ H ₁₂ O _{~6}) _n	~ 1000	SilvaChimica	FINTAN OP

(a)



(b)

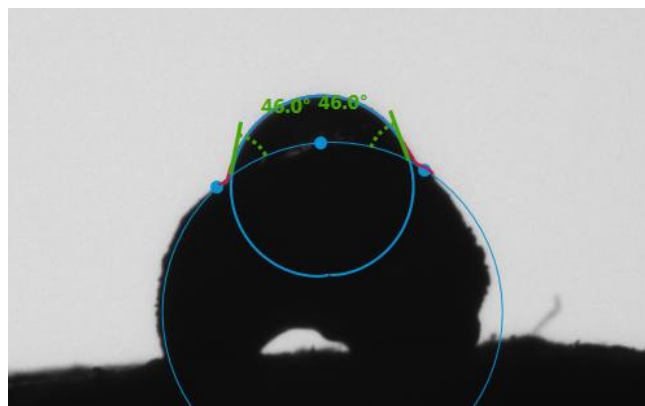


Fig. S11. Determination of the water contact angle of a droplet deposited on a spherical solid surface: (a) using a straight baseline and Eq. (1) where $\theta_{a,0}$ (°) is the true contact angle; (b) using a curved baseline.

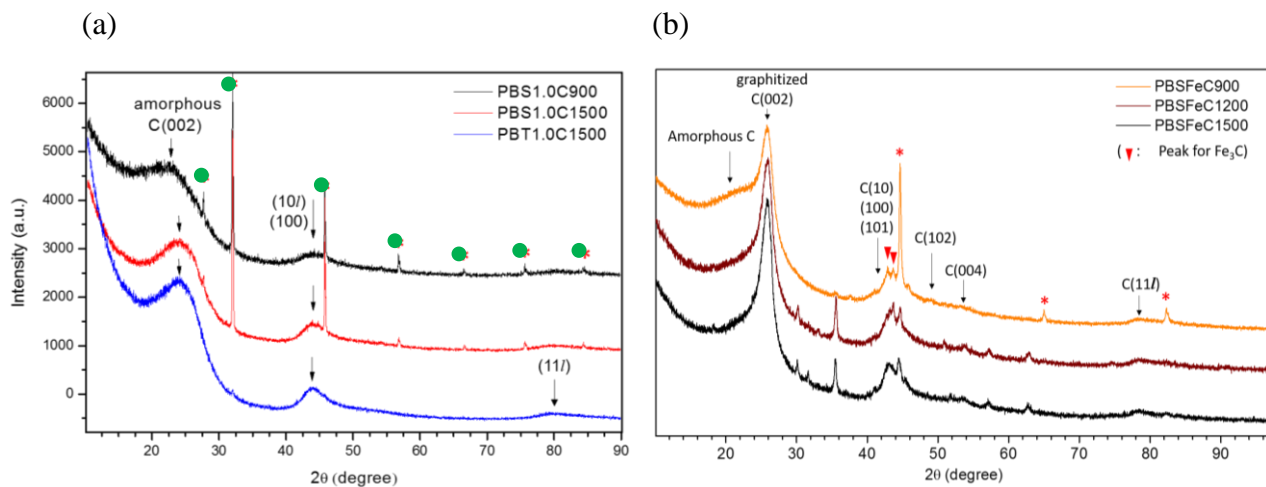


Fig. SI2. XRD patterns of: (a) PBS1.0C and PBT1.0C (i.e., metal-free HCSs derived from big templates with sucrose and tannin, respectively, as precursors) pyrolysed at different temperatures (900 and 1500°C); the green circles indicate the peaks of NaCl, present as impurity, in the case of HCSs tested after solar evaporation of salt water; and (b) PBSFeC (i.e., iron-loaded HCSs) pyrolysed at 900, 1200 and 1500°C (the red stars and triangles indicate the peaks related to metallic iron and to iron carbide, respectively).

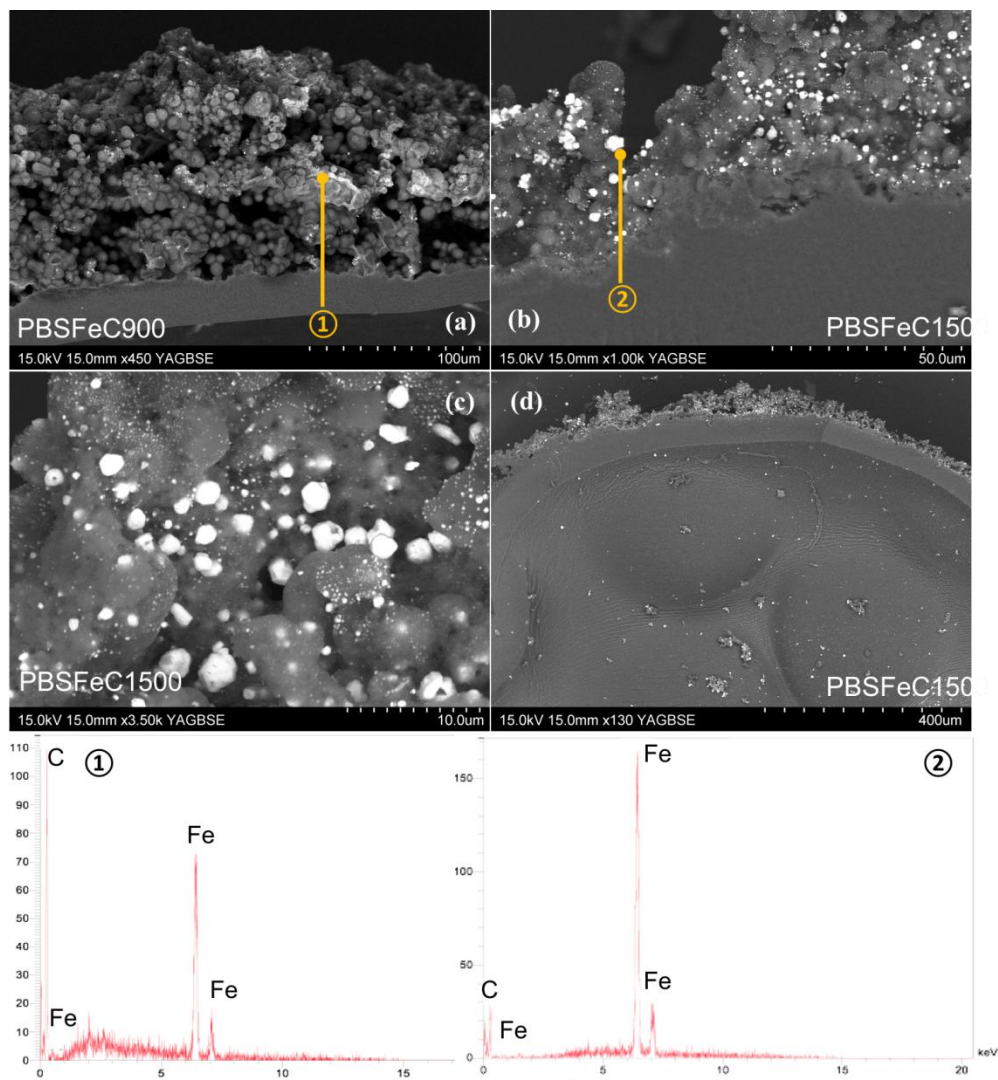


Fig. SI3. SEM images (top and middle rows) obtained with backscattered electrons of: (a) PBSFeC-900, and (b, c, d) PBSFeC-1500 at different magnifications and in which iron particles are seen as white spots, with local EDX analysis (bottom row) of two different points shown in (a) and (b).

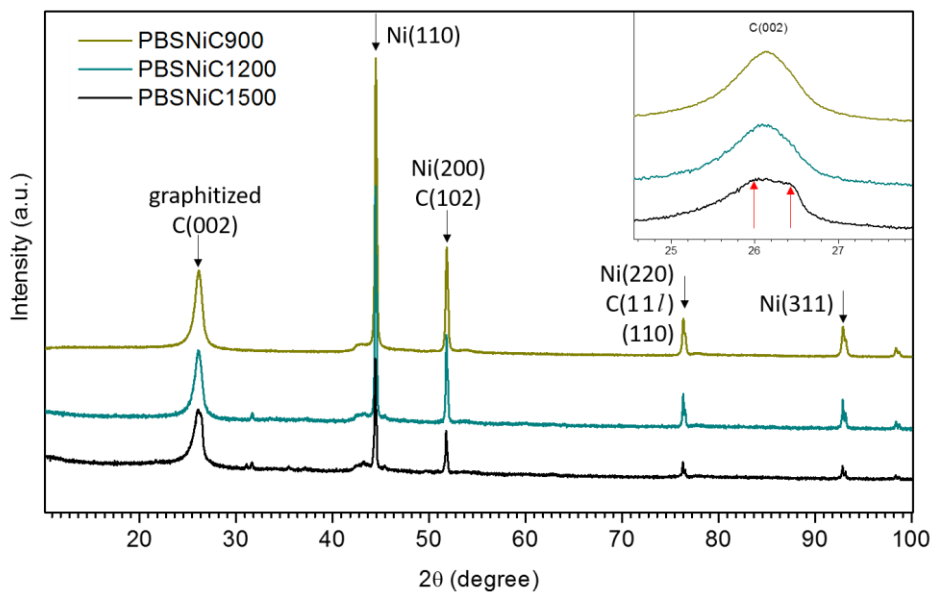


Fig. SI4. XRD patterns of PBSNiC (i.e., Ni-loaded HCSs) pyrolysed at different temperatures (900, 1200 and 1500°C). The inset is a zoom on the (002) reflection of carbon.

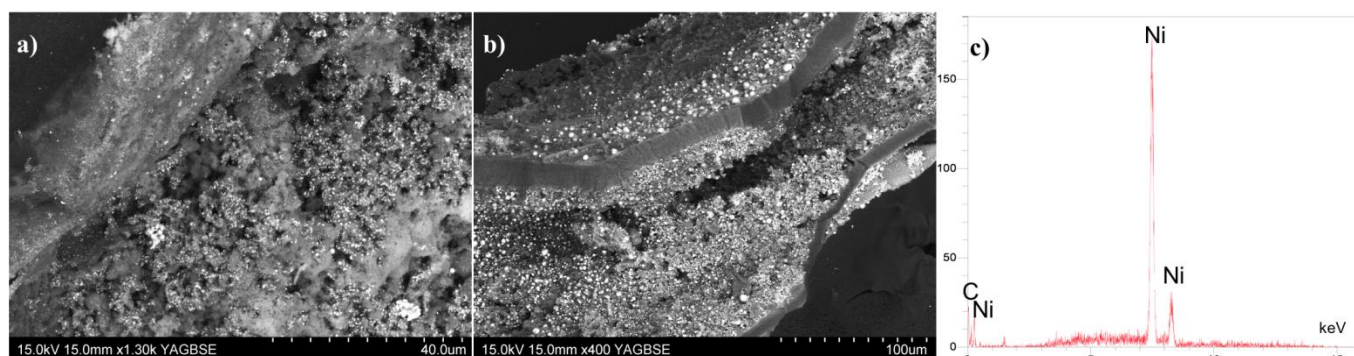


Fig. SI5. SEM images with backscattered electrons of: (a) PBSNiC-900, and (b) PBSNiC-1500 in which nickel particles are seen as white spots, and (c) the EDX analysis of one white spot in (a).

Table SI2. Structure analysis of metal-loaded HCSs prepared at different pyrolysis temperatures, based on XRD. θ_{002} is the Bragg angle, β is the line broadening at half the maximum intensity of the reflection, L_c is the crystallite size along c axis, and d_{002} is the interlayer spacing.

Sample name	$2\theta_{002}$ (°)	β (°)	L_c (pm)	d_{002} (pm)
PBSFeC900	25.829	0.0342	466	346
PBSFeC1200	25.872	0.0317	501	344
PBSFeC1500	25.872	0.0312	519	345
PBSNiC900	26.144	0.01878	844	340
PBSNiC1200	26.111	0.01878	939	341
PBSNiC1500	26.05/26.48	0.0141/0.0038	1140/3826	341/337

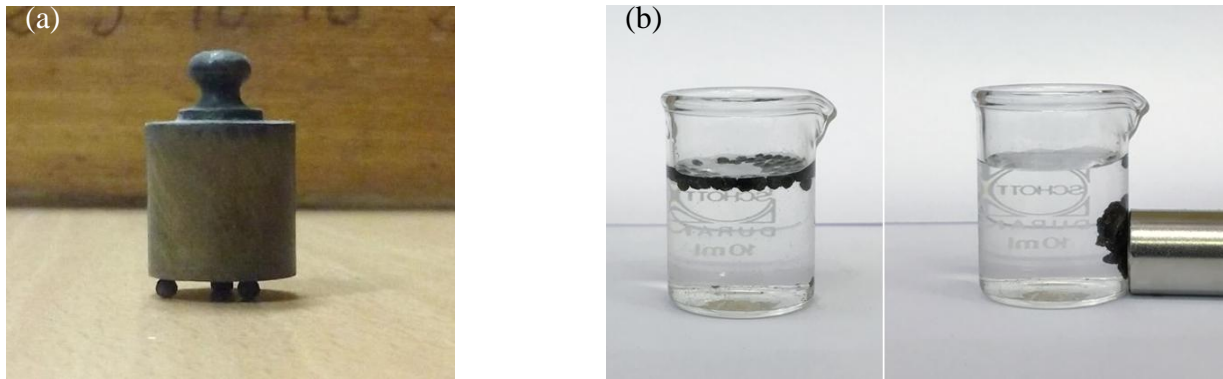


Fig. SI6. (a) Three HCSs of type PBS1.0C-900 submitted to compression with a 50g reference weight; (b) Strong attraction between metal-loaded HCSs and an Nd-based supermagnet (Supermagnete® N35, adhesion strength ~ 8.2 kg).

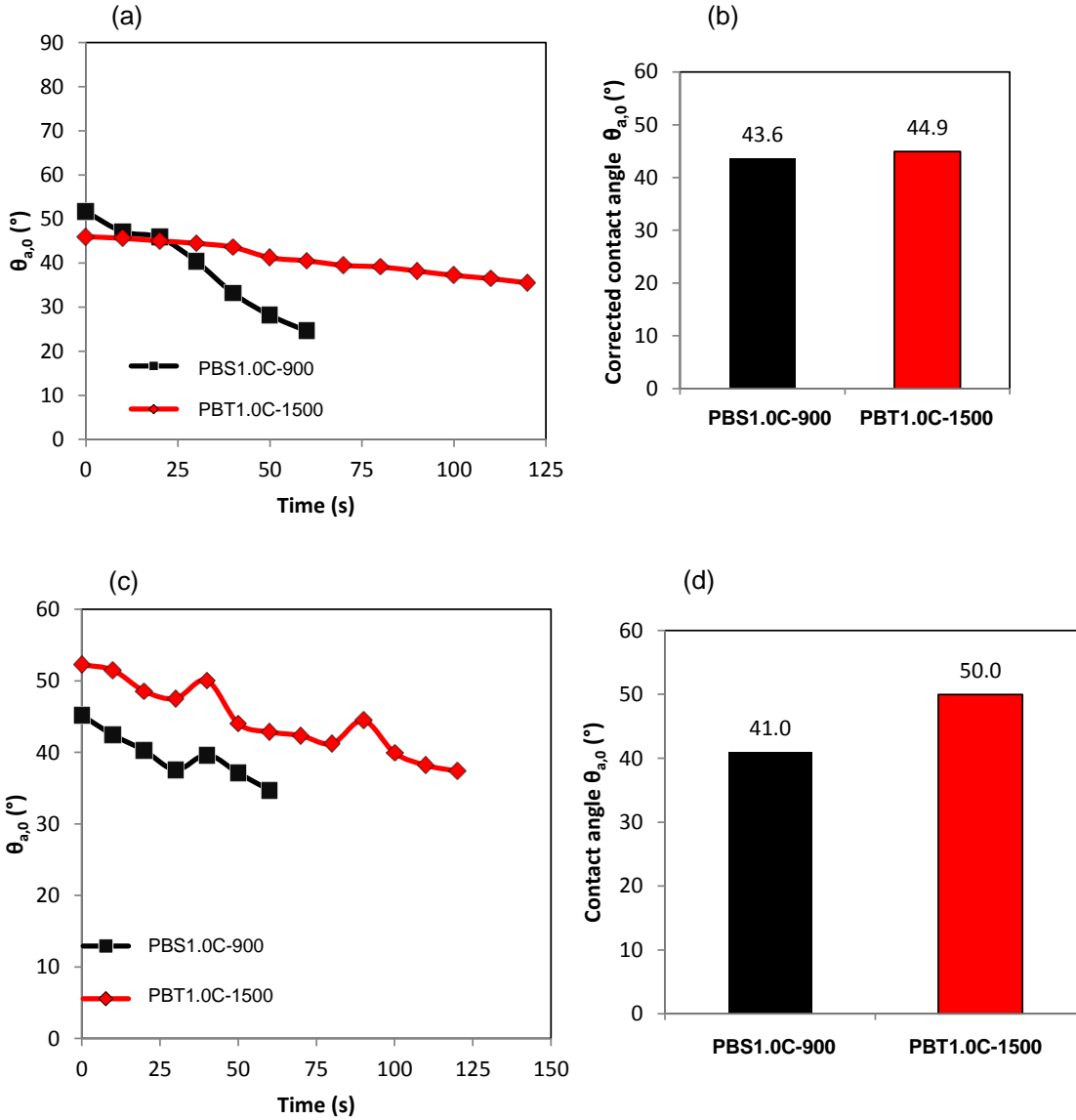


Fig. SI7. Contact angles of a few representative samples measured by two methods, using: (a-b) a linear baseline as shown in Fig. SI1a; (c-d) a curved baseline as shown in Fig. SI1b. (a and c) Time-dependent contact angle for two HCSs prepared from different precursors and pyrolysed at different temperatures, and (b and d) corresponding average contact angle 40 s after deposition of the water droplet.

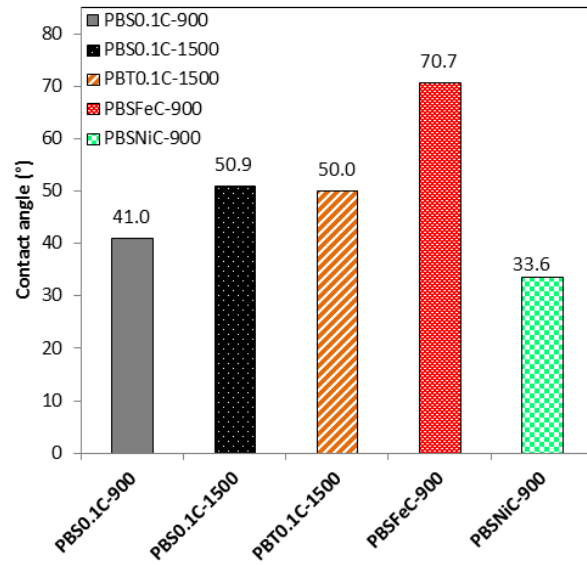


Fig. SI8. Average contact angles measured by the curved baseline method for a selection of HCSs.

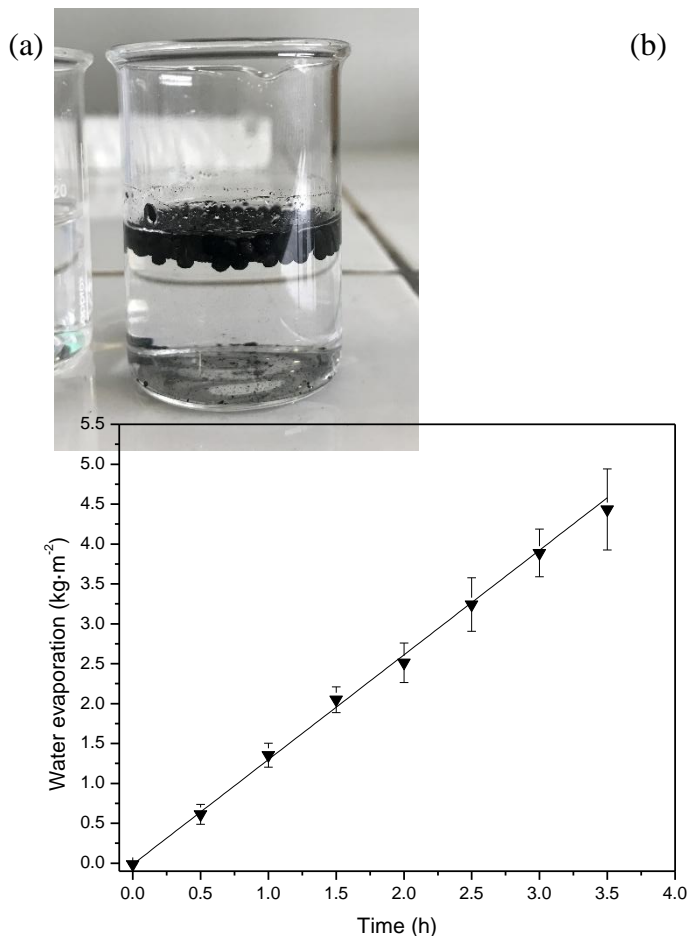


Fig. SI9. (a) PBS1.0C-900 hollow carbon spheres still floating three months after they were put at the surface of salt water; (b) Weight loss of an HCS-free beaker containing 20 g of 3.5 wt.% NaCl and submitted to a radiant power of 1 kW m^{-2} , as a function of time.

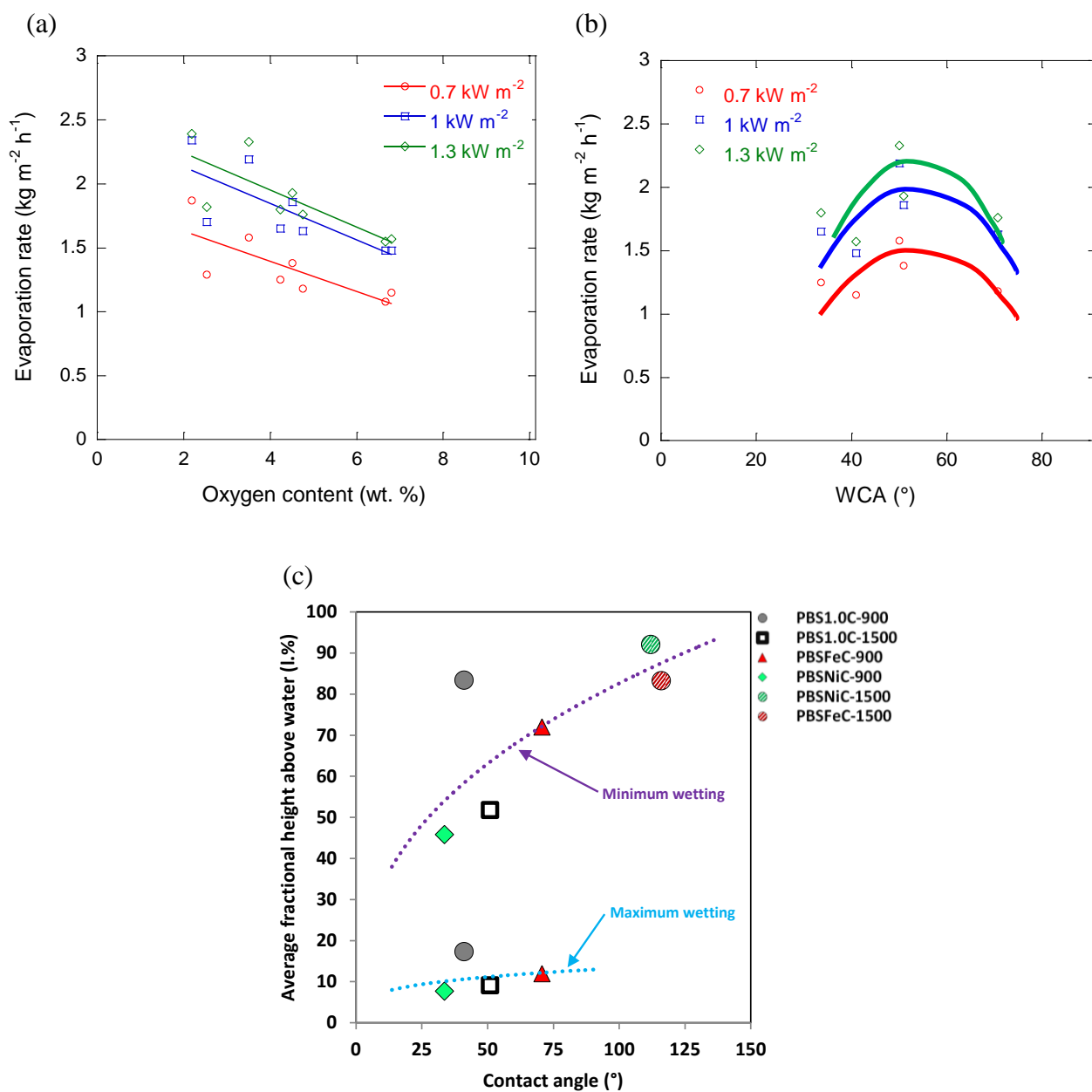


Fig. SI10. Changes of evaporation rate of salt water covered with HCSs as a function of their: (a) oxygen content; and (b) water contact angle, for each tested radiant power. (c) Correlation between floatability and contact angle for both cases of minimal and maximal wetting. The lines are linear fits in (a) but only guides for the eye in (b) and (c).

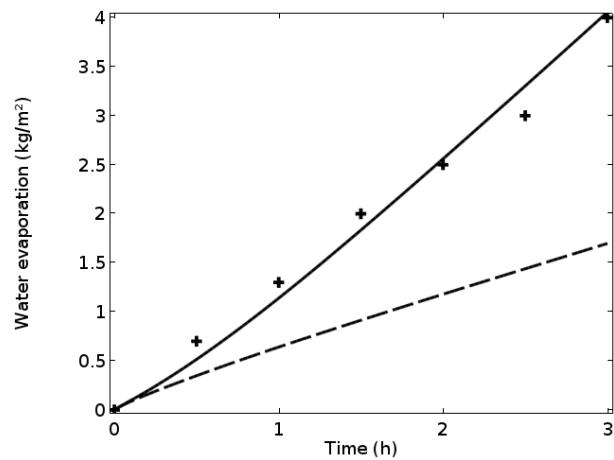


Fig. SI11. Experimental (crosses) and simulated (lines) evaporation rate (using a convective exchange coefficient $h_c = 47 \text{ W m}^{-2} \text{ K}^{-1}$) of the HCS-free system submitted to a radiant power of 1 kW m^{-2} , as a function of time: without (dashed line); and with a source term increasing linearly with the power of the solar simulator (solid line).

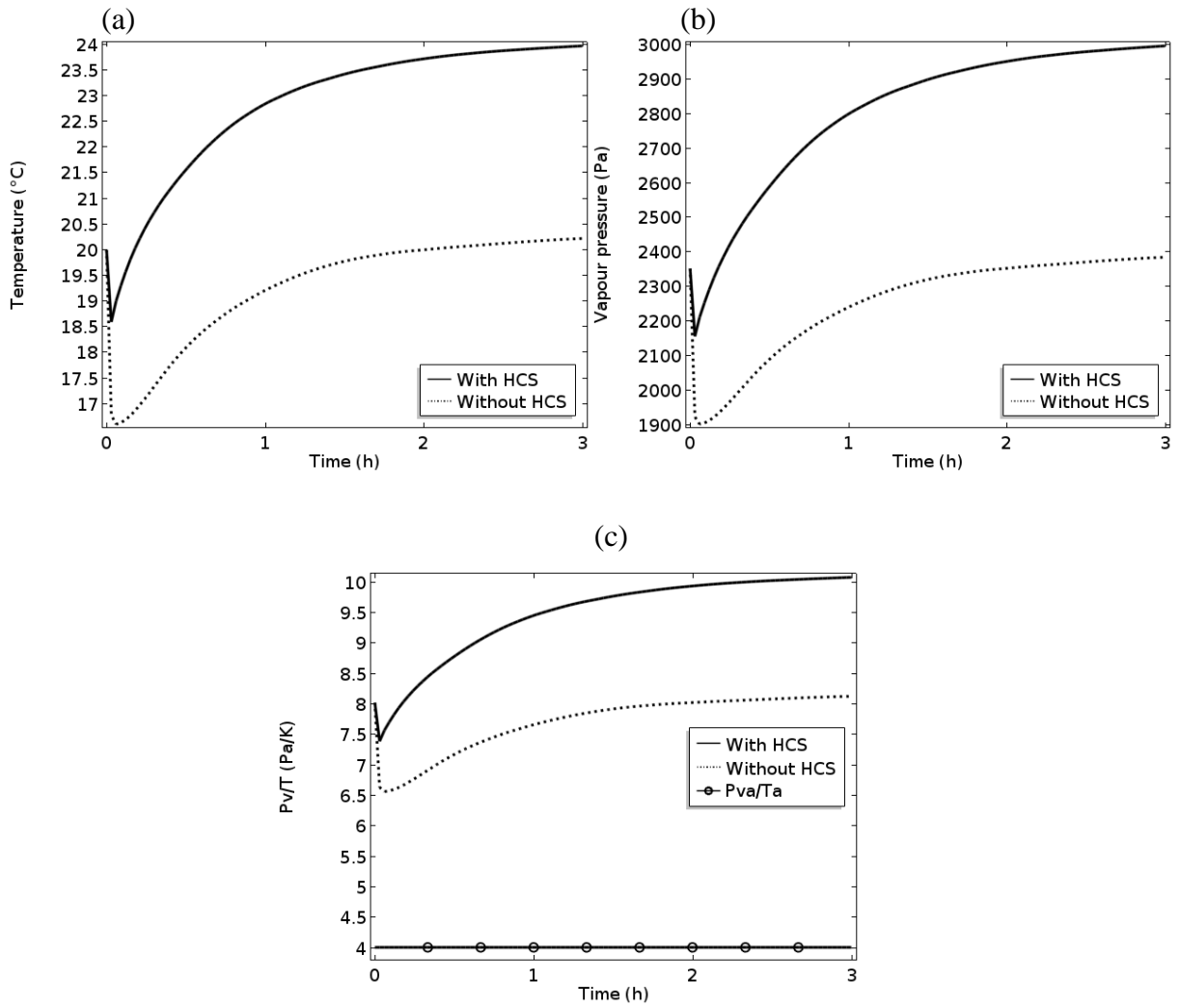


Fig. SI12. Impact on the presence of one HCS in the system (case #3 of Fig. 5b) on: (a) surface temperature; (b) surface water vapour pressure; and (c) p_v/T ratio (the index “a” referring to air), as a function of time.

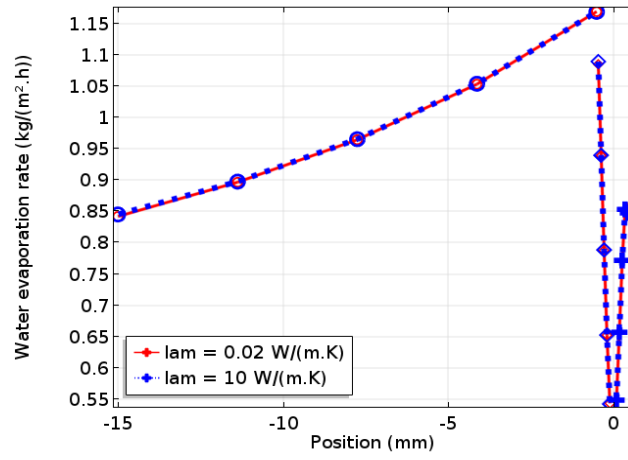


Fig. SI13. Same as Fig. 14, but the source term was set to zero.